THE IMPACT OF AXIAL PISTON MACHINES MECHANICAL PARTS CONSTRAINT CONDITIONS ON THE THERMO-ELASTOHYDRODYNAMIC LUBRICATION ANAL-YSIS OF THE FLUID FILM INTERFACES

Matteo Pelosi and Monika Ivantysynova

Purdue University, Department of Agricultural and Biological Engineering & School of Mechanical Engineering,
225 S. University St., West Lafayette, Indiana 47907, USA
mpelosi@purdue.edu, mivantys@purdue.edu

Abstract

The authors analyze the lubricating interfaces of axial piston machines considering thermo-elastohydrodynamic (TEHL) lubrication characteristics. The fluid film geometry in these conditions is strongly influenced by the surface elastic deformation of the solid boundaries. The surface elastic deformations derive from the high dynamic pressures developing in the fluid film, necessary to balance the external oscillating loads. Furthermore, elastic deflections of the fluid film develop from the thermal expansion of the solid bodies, caused by the heat generated due to viscous shear of the fluid film. The accurate determination of the solid boundaries elastic deformation is a key element to predict the fluid film geometry and consequently the lubricating interface performance.

When solving for the static elastic deformation of a solid body, constraint conditions must be imposed to avoid rigid body motion. Constraint conditions strongly influence the elastic deformation analysis; therefore their definition must reflect and interpret the mechanical body real conditions. In an axial piston machine all the mechanical bodies defining the fluid film geometry are loosely constrained and significant linear displacements and rotations are intentionally allowed. Hence, the definition of proper constraint conditions for the solid bodies is not a trivial problem and advanced constraint conditions must be considered and implemented.

In the fully-coupled numerical models of the lubricating interfaces developed by the research group of the authors, finite element analysis is used to determine the mechanical bodies' elastic deformations. The finite element analysis is coupled with finite volume models of the fluid film, to study the impact of the surface elastic deformations on the interfaces behavior. In this paper, the authors present and discuss the implementation of the inertia relief method on the finite element elastic deformation analysis of the main mechanical parts of an axial piston machine. Inertia relief allows simulating unconstrained structures in a static analysis using their inertia to resist the applied loads. Typical applications of this method include modeling an aircraft in flight, a submarine under water or a satellite in space. The impact of this method on the elastic deformation of the fluid film solid boundary surfaces is shown and compared to standard constraint conditions. In addition, the influence of the inertia relief method on the piston/cylinder interface fluid film behavior is discussed, presenting numerical results for a fully-coupled TEHL simulation over one shaft revolution of a special test pump capable of measuring the piston/cylinder axial viscous friction force. The improved accuracy of the piston/cylinder fully-coupled model including inertia relief effect is presented, comparing simulation results with friction force measurements.

Keywords: thermo-elastohydrodynamic lubrication, axial piston machine, inertia relief, constraint conditions, piston/cylinder interface

1 Introduction

The fluid film interfaces of an axial piston machines represent very complex tribological pairs and one of the rotating kit key design elements. The three main lubricating interfaces of an axial piston machine are shown in the cross section of Fig. 1. The three rotating kit

moving bodies are as well highlighted in Fig. 1. The fluid film behavior is characterized by the thermo-elastohydrodynamic lubrication, where the strong interactions between fluid and structures cannot be neglected. The lubricating interfaces are responsible for bearing the oscillating external loads and for sealing the high pressure regions of the machine. The moving

mechanical parts adjust their position continuously, in a periodic micro-motion, which induces a squeeze film effect to balance the external forces. In these conditions, the hydrodynamic pressure field developing in the fluid film causes the elastic deformations of the solid boundary surfaces (Huang and Ivantysynova, 2006). These deformations modify the fluid film geometry and the consequent elastohydrodynamic lubrication regime contributes to the overall load carrying capacity of the interfaces. In addition, during axial piston machine operation, the fluid film is continuously sheared by the relative motion of the mechanical bodies. The relative motion derives from the machine kinematics and the fluid film flow is considered as laminar under all possible normal operating points.
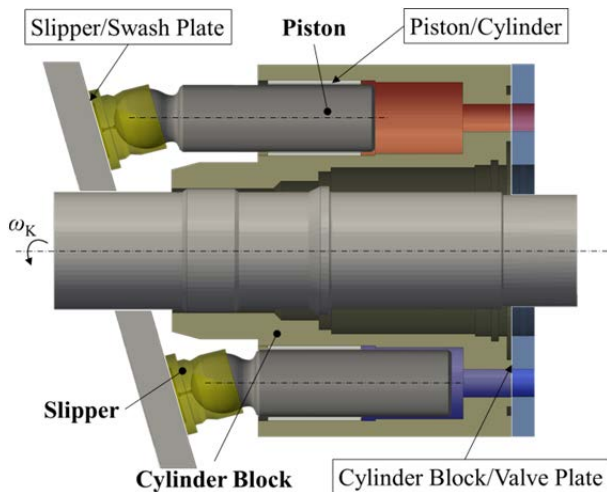
Fig. 1: *Axial piston machine three main fluid film interfaces*

The fluid film shear leads to viscous mechanical dissipations, which are translated into heat generation. Therefore, the solid parts temperatures are significantly increased. The thermal induced loads deriving from these temperature increments elastically deform the solid parts. Hence, the fluid film geometry is further modified by thermal surface elastic deformations (Pelosi and Ivantysynova, 2009).

The accurate determination of the surface elastic deformations is therefore crucial to predict the exact fluid film geometry and the lubricating interfaces behavior.

In general, the calculation of the elastic deformation of a solid body subjected to complex external and thermal static loads is strongly influenced by its constraint conditions. As previously illustrated, the main mechanical bodies of the rotating kit of an axial piston machine are designed to allow a relative kinematic motion between the parts and a micro metric interface movement. This latter motion is responsible for the squeeze film effect and for an increased fluid film load carrying ability. Hence, the definition of proper constraint conditions for the mechanical parts is a challenging problem and also design dependent.

To improve the elastic deformation analysis of axial piston machine mechanical parts, the authors implemented and investigated the impact of an advanced method. This method, known as inertia relief, strongly reduces the influence of the constraint conditions on the

solution of the linear elastic problem. This technique assumes that applied forces and torques are balanced by inertial forces induced by an acceleration field (Hintz, 1975). The acceleration field precisely cancels the applied loads. The method therefore allows simulating unconstrained structures in an elastic static analysis, assuming that the solid structure is in a state of static equilibrium even though it is not physically constrained. Typical applications of inertia relief include modeling an aircraft in flight, a submarine under water or a satellite in space.

In this paper, the motivation for the implementation of the inertia relief method and its numerical characteristics are discussed. The inertia relief method extends the capabilities of the thermal and fluid-structure interaction models for the axial piston machine fluid film interfaces developed by the research group of the authors. An overview of these models is given in the next sections of this paper, focusing on the finite element modeling used to determine the mechanical parts elastic deformations.

Numerical results are presented, discussing the influence of the inertia relief method on the elastic deformation of the rotating kit main solid bodies. Furthermore, considering a special design test pump capable of measuring piston/cylinder friction forces, results from a fully coupled piston/cylinder interface simulation over one shaft revolution are shown. The impact of the inertia relief method on the prediction of piston/cylinder axial friction forces is discussed, by comparing the simulation results with friction force measurements.

2 Mechanical Parts Dynamic Load Conditions and Micro-Motion

To allow for the relative motion between the rotating kit mechanical bodies and to achieve the desired machine kinematics, adequate play is allowed and precise clearances for the fluid film interfaces are engineered. During axial piston machine operation, two different types of motion of piston, slipper and cylinder block can be distinguished, directly affecting the respective fluid film behavior. A macro-motion derives from the relative movement between the parts and can be described by the machine kinematic characteristics. A micro-motion arouses from the extremely transient oscillating load conditions acting on the solid bodies and periodically squeezes the fluid film. In fact, during one shaft revolution of the machine, the displacement chamber pressure changes depending on the machine kinematics and timing. This pressure induces the main oscillating loads acting on the solid bodies and causes a transient loading condition.

The fluid film interfaces hydrodynamic behavior is responsible for bearing these oscillating loads, generating sufficient fluid film pressure to fully balance the external forces and to avoid metal to metal contact. In addition, the high degree of freedom characterizing the mechanical parts and their self-adjustment motion is responsible for a squeeze film pressure build up. This

tribological effect, induced by the parts micro-motion, strongly improves the load carrying ability of the fluid film interfaces and cannot be neglected when studying the fluid film behavior of axial piston machines.

For example, considering the piston/cylinder interface, the varying external forces acting on the piston are presented in Fig. 2 (Ivantysyn and Ivantysynova, 2001). Due to the machine kinematics, the piston slides axially in a reciprocating motion. In addition, the piston rotates about its axis with an angular speed comparable to the shaft speed. The pressure force, F_{DK}, resulting from the displacement chamber pressure represents the main load acting on the piston body. In addition, piston inertia force, F_{aK}, and piston friction force, F_{TK}, change their magnitude periodically over one shaft revolution. The resulting swash plate reaction force, F_{SK}, is also oscillating and creates a side force, F_{SKy}, acting on the piston.

F_{DK}: Pressure force
F_{SK}: Swash plate reaction force
F_{SKy}: Swash plate reaction side force
F_{TK}: Viscous friction force
F_{aK}: Piston inertia force
$F_{ωK}$: Piston centrifugal force
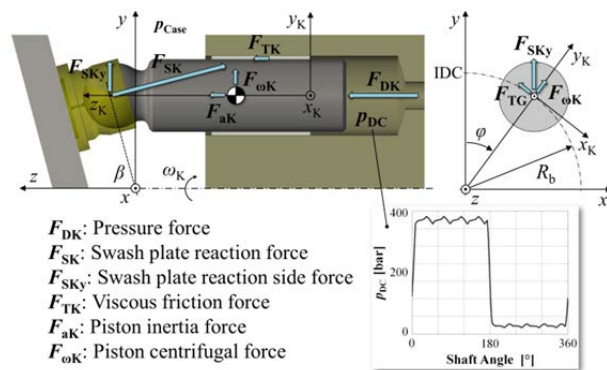
Fig. 2: *Piston oscillating forces and piston/cylinder coordinate systems*

The side load, F_{SKy}, mainly contributes to the piston micro-motion and to the dynamic piston eccentricity oscillation. This changing eccentricity of the piston induces a squeeze film effect and results in a dynamic fluid film pressure field which balances all the external forces and moments. Therefore, the piston performs a micro-motion, self-adjusting its eccentricity by varying the squeeze motion to balance the oscillating external loads.

Similar dynamic considerations can be drawn for the other moving parts of the rotating kit: the slipper and the cylinder block. Hence, during one shaft revolution of the machine, all the rotating kit moving mechanical bodies are subjected to a complex transient loading condition while not being firmly constrained.

This design characteristic represents a significant issue when performing numerical analysis to predict the solid bodies elastic deformations. In the lubricating interfaces of an axial piston machine a thermo-elastohydrodynamic lubrication regime, introduced in the next paragraphs, typically develops. In this condition, the surface elastic deformations of the solid bodies and the consequent fluid film thickness modifications are critical to determine the lubricating interfaces performance. Therefore, an advanced method to reduce the impact of the constraint conditions on the solids static deformation analysis is necessary: the inertia relief method.

3 Thermo-Elastohydrodynamic Fluid Film Lubrication Conditions and Modeling

In the complex dynamic loading scenario, affecting the rotating kit mechanical bodies, several physical phenomena take place and influence the fluid film interfaces behavior. The flow in the fluid film is considered laminar under all possible normal operating points. The relative motion between the parts contributes to develop hydrodynamic pressure in the fluid film interfaces. Moreover, the squeeze film effect due to the solid parts micro-motion induces local high pressure peaks in the fluid film. This dynamic fluid film pressure distribution causes the elastic deformation of the solid boundaries, acting as a significant external load on the mechanical parts surfaces. These elastic deformations lead to an elastohydrodynamic lubrication regime and introduce a fluid-structure interaction problem involving mechanical solids of complex design. In fact, the geometrical characteristics and spatial extension of the fluid film interfaces do not allow simplifications in the tribological analysis.

A second important phenomenon taking place in the interfaces is connected to the energy dissipated in the film due to the viscous shear of the fluid. The relative motion of the solid parts in fact causes a viscous mechanical dissipation, which generates heat. The heat alters the temperature distribution of the solid parts and significantly increases the machine operating temperature. Irregular solids temperature fields represent a complex boundary for a non-isothermal fluid flow analysis. Furthermore, temperature increments in the solids translate into internal thermal stresses. Thermal induced loads elastically deform the solid bodies contributing to additional fluid film thickness modifications.

Therefore, a thermo-elastohydrodynamic lubrication regime characterizes the fluid film interfaces performance (Kim and Sadeghi, 1993). The precise analysis of such a complex physical scenario requires the development of advanced numerical models. For this reason, the research group of the authors developed fully coupled fluid-structure interaction and thermal models for the three main lubricating interfaces. The models combine the solution of the non-isothermal fluid film flow with the solid boundaries behavior (Pelosi and Ivantysynova, 2010).

In the next paragraphs, an overview of the structure of the simulation model for the lubricating interfaces is given. The model couples different numerical techniques and algorithms to consider the different physical effects influencing the fluid film. Particular attention will be given to the description of the finite element model used to determine the solid parts elastic deformations. This is essential to introduce the inertia relief method, its implementation and impact on the finite element analysis.

3.1 Fully Coupled Fluid-Structure Interaction & Thermal Model

The model combines different computational strategies and discretization techniques to address and to solve all the considered fluid film physical phenomena. Referring to Fig. 3, an overview of the numerical tools coupled to solve for the piston/cylinder interface thermo-elastohydrodynamic regime is given. Similar numerical strategies are adopted for the other fluid film interfaces. In particular, finite volume models of the fluid film determine the interface pressure, p, and temperature, T, distribution, solving the Reynolds and energy equations respectively. The heat transferred from the fluid film to the solid parts, Q_S, is used as a boundary for unstructured finite volume models of the mechanical bodies to determine their temperature distribution, T_B. The elastic deformations due to pressure and temperature loads are determined using finite element analysis on hexahedron or tetrahedron based meshes of the solid parts. The fluid film surface elastic deflections, Δh, are therefore considered in the fluid film thickness definition.
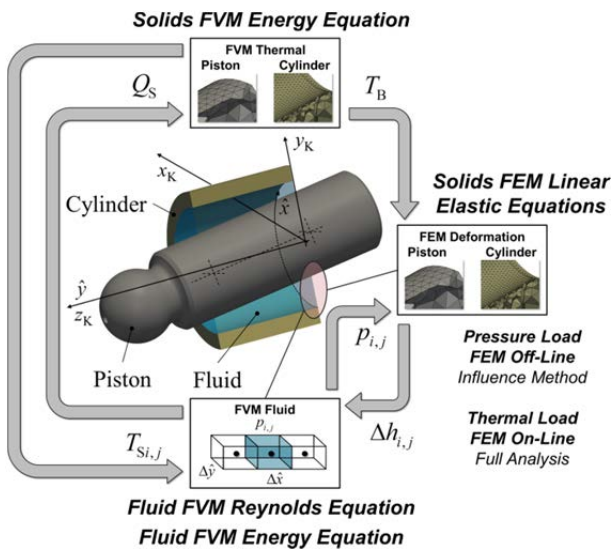
Fig. 3: *The piston/cylinder fluid-structure and thermal fully coupled model*

An external fixed-point iterative coupling between fluid and solid domains solves for the mutual interactions. The three main numerical environments are briefly discussed in the following sections, reporting the main implemented equations and computational strategies for the piston/cylinder interface.

3.1.1 Non-Isothermal Fluid Film Finite Volume Flow Model

The fluid film behavior is analyzed through the simultaneous solution of the Reynolds and of the energy equations. The change in fluid properties due to pressure field and temperature field are considered. The Reynolds equation, which predicts the fluid film pressure field, is shown in is general form in Eq. 1.

$$-\nabla \cdot \left(\frac{h^3}{12\mu} \nabla p \right) + \frac{\boldsymbol{V}}{2} \cdot \nabla h + \boldsymbol{V} \cdot \nabla h + \frac{\partial h}{\partial t} = 0 \qquad (1)$$

The Reynolds equation is discretized on a finite volume domain and is solved using a geometric multigrid method (Pelosi and Ivantysynova, 2010).

The solution of the energy equation allows calculating the fluid film temperature distribution. On a finite volume domain, a convective-conductive form of the energy equation, Eq. 2, is solved using a SOR Gauss-Seidel scheme.

$$\rho c_{\mathrm{p}}\, \boldsymbol{V} \cdot \nabla T = \nabla \cdot \left(\lambda\, \nabla T \right) + \mu\, \Phi_{\mathrm{D}} \qquad (2)$$

The energy equation presents a source term, Φ_{D}, which is a quadratic function of spatial derivatives of fluid velocity components, as shown by Eq. 3 in Cartesian coordinates (Ivantysynova, 1985).

$$\Phi_{\mathrm{D}} = 2\left[\left(\frac{\partial u}{\partial x} \right)^2 + \left(\frac{\partial v}{\partial y} \right)^2 + \left(\frac{\partial w}{\partial z} \right)^2 \right] + \left(\frac{\partial u}{\partial y} + \frac{\partial v}{\partial x} \right)^2 +$$
$$+ \left(\frac{\partial v}{\partial z} + \frac{\partial w}{\partial y} \right)^2 + \left(\frac{\partial w}{\partial x} + \frac{\partial u}{\partial z} \right)^2 - \frac{2}{3} \left(\nabla V \right)^2 \qquad (3)$$

The function gives the rate at which mechanical energy is converted into heat in a viscous fluid per unit volume. The solution of the energy equation allows determining the heat fluxes generated in the fluid film to the solid bodies. The fluid film heat fluxes are the key boundary for the determination of the solid bodies temperature distribution.

3.1.2 Solid Bodies Finite Volume Heat Transfer Model

The fluid film viscous shear due to the solid parts macro motion is responsible for the tribological interfaces mechanical dissipation. This energy is transferred from the fluid film to the mechanical bodies in form of heat flux, generating significant temperature gradients in the solid parts, which are therefore characterized by complex uneven temperature distributions (Pelosi and Ivantysynova, 2009).

The development of detailed heat transfer models of the solid bodies is important to obtain an accurate prediction of their temperature fields. The knowledge of these temperatures allows implementing a more precise temperature boundary for the fluid film surfaces, improving the results of the non-isothermal fluid flow calculations. The three dimensional temperature distributions in the solid bodies are not only used as a better boundary for the fluid film but also to determine the thermal loading conditions, which cause fluid film thickness alterations due to temperature induced surface elastic deformations.

$$\nabla \cdot \left(\lambda \nabla T \right) = 0 \qquad (4)$$

The in-house developed heat transfer models are based on an unstructured finite volume discretization of the solid parts, while the solution of the diffusive temperature equation (Eq. 4) is achieved using an over-relaxed Gauss-Seidel (SOR) iteration scheme. To obtain a high level of accuracy in the prediction of the solid temperatures, the thermal diffusive equation solver is able to handle unstructured discretization of the solid domains (Murthy, 2002). The solid bodies are therefore directly analyzed from CAD drawing of the

machine and discretized using powerful external meshing software, *Altair HyperMesh*, as shown in Fig. 4.
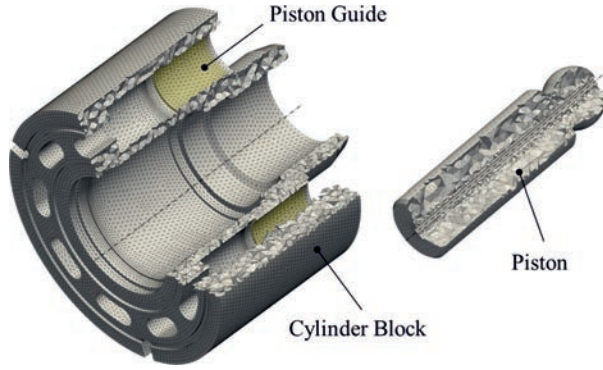
Fig. 4: *The cylinder block and piston unstructured finite volume discretization*

First order elements, such as tetrahedrons or hexahedrons can be implemented. During the external meshing process, the proper boundary conditions for the thermal calculations are set by the user, together with the specification of the different material properties. The thermal solver can in fact handle different materials combinations, being axial piston machine design often characterized by the presence of components having different material properties as well as various types of coatings.

3.1.3 Solid Bodies Finite Element Elastic Deformation Model

Based on the external loads due to fluid film pressure and on the internal loads due to solids temperature a finite element elastic model determines the elastic deformation of the solids. Similarly to the heat transfer module, the finite element analysis is based on external meshing of tetrahedrons or hexahedron elements. The user specifies loaded surfaces, constrained nodes and material properties. The finite element analysis, which will be theoretically discussed in depth in the next paragraphs, is based on the solution of the linear system of elastic equations, reported in Eq. 5.

$$\mathbf{K} \cdot \boldsymbol{u}_\mathrm{d} = \boldsymbol{F}_\mathrm{E} + \boldsymbol{F}_\mathrm{T} \qquad (5)$$

In this form, the elastic nodal deflection of the solid body mesh, $\boldsymbol{u}_\mathrm{d}$, is in direct proportion with the pressure external nodal loads, $\boldsymbol{F}_\mathrm{E}$, and the temperature internal loads, $\boldsymbol{F}_\mathrm{T}$, applied to it. $\mathbf{K}$ represents the master stiffness matrix of the solid body, function of material and discretization properties. The solution of the master linear system of equations for $\boldsymbol{u}_\mathrm{d}$ is obtained using a conjugate gradient iterative method.

Two different methods to determine the final elastic deformation are employed according to the type of load. The solution of pressure surface elastic deformation is obtained using an influence method, running complete FEM analysis off-line. On the other side, the solution of the thermal deformation is achieved running a complete FEM analysis run-time (Pelosi and Ivantysynova, 2009).

In fact, since the deformation due to pressure loading must be recalculated at each of the Reynolds equation iterative steps being directly connected to the lu-

bricating film dynamic pressure field, solving the complete finite element analysis at this rate would make the simulation time unacceptable. Therefore, an influence method scheme is implemented. Using the integrated FEM code, a set of influence matrices for the solid bodies is calculated off-line. Before executing the fully-coupled simulation, considering for example the piston/cylinder interface, separate sets of influence matrices are generated for the piston and cylinder bodies. In particular, each face of the solid surface defining the fluid film boundary is loaded with a reference pressure of 100 bar. Each influence matrix corresponding to the loaded face contains the elastic deformation of the entire surface. Furthermore, the surface elastic deformation due to a reference displacement chamber pressure of 100 bar acting on the surfaces exposed to p_DC is also calculated. Referring to Fig. 5, an influence matrix for the piston is shown, where the deformation field due to the reference load acting on one surface element face is represented.
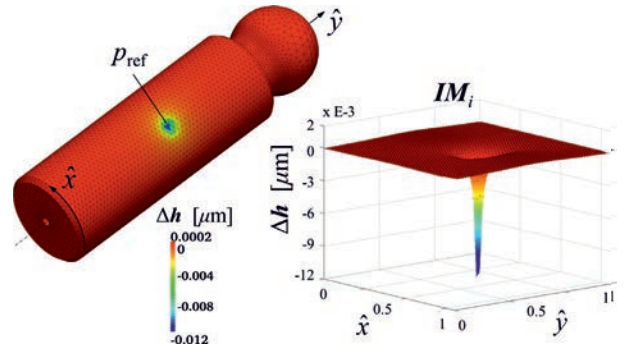
Fig. 5: *Influence matrix IM_i for i^th piston surface element*

During simulation, depending on the actual dynamic pressure field and boundary pressures, the solid body surface elastic deformation is determined based on Eq. 6.

$$\Delta \boldsymbol{h} = \sum_{i=1}^{N} \frac{p_i}{p_\mathrm{ref}} \boldsymbol{IM}_i + \frac{p_\mathrm{DC}}{p_\mathrm{ref}} \boldsymbol{IM}_\mathrm{DC} \qquad (6)$$

Where $\Delta \boldsymbol{h}$ is the array containing the elastic deflection of each of the surface nodes of the solid domain, p_i is the external fluid pressure acting on each of the N faces of the loaded surface. Furthermore, $\boldsymbol{IM}_i$ is the ith face influence matrix, containing the elastic deformation of all the surface nodes, when the ith face is loaded with a reference pressure p_ref. $\boldsymbol{IM}_\mathrm{DC}$ is the influence matrix containing the elastic deformation of all the surface nodes from displacement pressure load. The influence method is based on the superimposition principle, valid since the deformation is assumed to take place in the elastic region. Thanks to this method, the FEM surface elastic deformation calculations reduce to matrix addition and multiplication, dramatically reducing the solution time. Further acceleration of the process is obtained through parallel computing of the $\Delta \boldsymbol{h}$ vector.

3.1.4 Fluid-Structure Interaction

The communication between fluid domain and structure domain is complicated by two separate caus-

es. The first problem is the difference in the fluid discretization and the solid discretization. The fluid film is discretized using a regular structured grid, while the solids are discretized using typically an unstructured mesh. The second issue is related to the relative motion presented by the solid parts, which causes the fluid film to face a continuously changing solid boundary. For these reasons, an advanced interpolation scheme has been implemented between the fluid and structure domain, based on the relative position of the respective cells centroids. Pressure and heat are interpolated from the fluid film to the structures, while surface elastic deformations and temperatures are interpolated from the structures to the fluid film.

The interpolation method is based on a very efficient approximate nearest neighbor searching. The search finds for each query point, q, a set of P nearest points and respective square distances, d^2. With this information, a modified inverse distance weighting interpolation is implemented, also known as modified Shepard's method. In particular, for a given query point the interpolated value, F_q, from the neighbors' values, f_i, can be expressed as:

$$F_q(x, y, z) = \sum_{i=1}^{P} w_i \cdot f_i(x, y, z) \qquad (7)$$

Where, the weight functions w_i are each function of Euclidean distance and are radially symmetric about each neighbor point. As a result, the interpolating surface is symmetric about each point. The weight functions are defined as follows for each neighbor point:

$$w_i = \frac{\left[\dfrac{R - d_i}{R d_i}\right]^2}{\sum_{j=1}^{P}\left[\dfrac{R - d_j}{R d_j}\right]^2} \qquad (8)$$

Where, R is the distance between the query point and the most distant neighbor.

3.1.5 Fully Coupled Numerical Algorithm

The complete solution scheme can be described referring to Fig. 6. A shaft revolution of the machine is simulated, solving in time at discrete intervals, corresponding to a progressively increasing shaft rotation and different load conditions (Pelosi and Ivantysynova, 2009). The core of the algorithm is represented by the thermo-elastohydrodynamic fluid film described so far. The Reynolds and the energy equations are solved on a finite volume discretized domain. The non-isothermal fluid film flow equations are solved iteratively by the most inner loop. The fluid properties and the surface elastic deformation due to the dynamic pressure field are updated at each iteration step. The piston and cylinder solids surface elastic deformation is calculated via an influence method, where a set of influence matrices for the solid bodies is calculated running an off-line finite element analysis. The fluid dynamic pressure field and the solid boundaries surface elastic deformation are strongly related, making the problem non-linear and the numerical solution extremely delicate

and stiff. The problem is treated as a partitioned fluid-structure interaction analysis, where the non-linearity is incorporated by an outer iterative Picard scheme. Hence, the pressure-deformation convergence is obtained using a smart under-relaxed fixed point Picard iteration, which adjusts the under-relaxation coefficients proportionally to the pressure residual behavior.
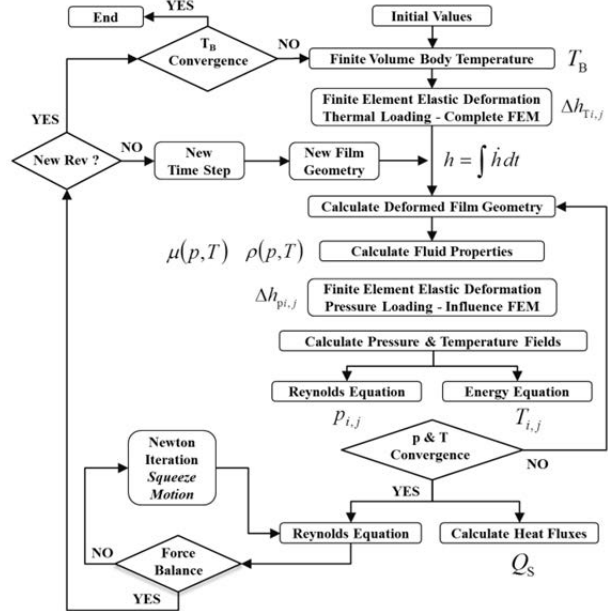
Fig. 6: *The complete fully-coupled solution algorithm*

Once a converged solution for the instantaneous fluid-structure interaction problem is reached, a numerical scheme based on a Newton-Raphson root finding, varies the piston squeeze velocity to achieve a load balanced condition, as developed by Wiezcorek and Ivantysynova (2002). In fact, the fluid film pressure field must balance the external loads acting on the moving body. When a balanced condition is reached, the proper squeeze motion is integrated using a first order fixed time step Eulerian integrator. A new eccentric position in the next simulation time step is found. This scheme repeats itself until the end of one shaft revolution. In addition, at each simulation step the thermal conductive fluxes from the fluid film to the solid bodies are calculated. At the end of the revolution, the averaged heat fluxes are used to determine the solid parts temperature distribution, using the finite volume heat transfer models. These temperatures are used in the following revolution as a more accurate boundary condition for non-isothermal fluid film flow calculations and to predict fluid film thickness variations due to solids thermal expansions through a complete finite element analysis. The most outer loop continues to iterate over few shaft revolutions until stable temperature distributions in the solid bodies are reached.

4 Inertia Relief Method in FEM

The determination of the mechanical parts surface elastic deformations is crucial to predict the correct fluid film geometry. As previously described, the elastic deformation of the solid bodies is calculated using a

finite element analysis. The numerical solution of the linear system of elastic equations, Eq. 5, needs the definition of sufficient constraint conditions to prevent rigid body motion. In fact, when performing an elastic deformation analysis a sufficient number of boundary (constraint) conditions must be imposed to avoid rigid body motion and rotation. In addition, the constraints definition should replicate the mechanical body real conditions. In supporting a three dimensional body, the minimal number of degrees of freedom (DOFs) that have to be constrained is six and many combinations are possible. Essential Zero Dirichlet constraint conditions have to be defined to avoid rigid movements. In particular, assuming boundary values of zero (no displacement for the constrained nodes), allows for a reduction in the linear system of equations by removal of rows and columns associated with those zero displacements. A unique solution for the displacement vector can be therefore found.

A proper definition of the constraint conditions is therefore fundamental both numerically, to obtain a unique solution of the linear system, and physically, to reproduce the mechanical part real environment. The main rotating kit mechanical parts present a relative macro-motion and are designed to perform a squeeze film micro-motion. The squeeze film effect plays a key role in ensuring fluid film hydrodynamic pressure build up and sufficient interface load carrying ability. Therefore, the solid bodies forming the core of an axial piston machine are loosely constrained, introducing a significant numerical issue when dealing with their finite element elastic deformation analysis. For these reasons, an advanced method has been implemented to strongly reduce the impact of the constraint conditions on the elastic deformation solution, referred to as the inertia relief method. This technique allows simulating unconstrained structures in an elastic static analysis. It is assumed that the solid structure responds to the applied loads with its inertia and, for this reason, can be defined in a state of static equilibrium even though it is not physically constrained. All the applied forces and torques reduced to the body center of mass (CG) are balanced by inertial forces and moments induced by an inertial acceleration field.

In the next paragraphs, the inertia relief method and its mathematical coupling with the developed finite element analysis will be presented.

4.1 Elastic Finite Element Analysis

The elastic deformation of the solid bodies is analyzed for one single element and then extended to the rest of the numerical domain (Hartley, 1986). The minimum potential energy principle is the fundament of the finite element analysis developed and implemented in the model. Based on this principle and considering only element nodal forces derived from external pressure loads and from internal thermal stress, the total potential energy in the single element system consists of the element strain energy, U_ε, and the external loads energy potential, V_{NF}. Therefore, the total potential energy in the element, Π, can be expressed as follows:

$$\Pi = U_\varepsilon + V_{NF} =$$

$$= \frac{1}{2} \int_{\Delta V_0} (\mathbf{B}\, \boldsymbol{u}_d - \boldsymbol{\varepsilon}_T)^T \mathbf{C} (\mathbf{B}\, \boldsymbol{u}_d - \boldsymbol{\varepsilon}_T)\, dV - \boldsymbol{u}_d^T \begin{Bmatrix} F_{x1} \\ F_{y1} \\ F_{z1} \\ \vdots \\ F_{xn} \\ F_{yn} \\ F_{zn} \end{Bmatrix} \quad (9)$$

Where $\boldsymbol{\varepsilon}_T$ is the temperature induced strain, $\mathbf{B}$ is the strain-displacement matrix and $\mathbf{C}$ represents the constitutive matrix for an isotropic material. Assuming that of all the possible deformed configurations, the element will assume the one corresponding to its minimum total potential energy, Π is minimized relative to the nodal vector $\boldsymbol{u}_d$. Differentiating the energy with respect to each displacement and setting each resulting equation equal to zero yields to the matrix equation of elasticity.

$$\mathbf{k}^T \boldsymbol{u}_d = \int_{\Delta V_0} \mathbf{B}^T \mathbf{C} \mathbf{B}\, dV \begin{Bmatrix} u_{x1} \\ u_{y1} \\ u_{z1} \\ \vdots \\ u_{xn} \\ u_{yn} \\ u_{zn} \end{Bmatrix} =$$

$$(10)$$

$$\begin{Bmatrix} F_{x1} \\ F_{y1} \\ F_{z1} \\ \vdots \\ F_{xn} \\ F_{yn} \\ F_{zn} \end{Bmatrix} + \int_{\Delta V_0} \mathbf{B}^T \mathbf{C}\, \boldsymbol{\varepsilon}_T dV = \boldsymbol{F}_E + \boldsymbol{F}_T = \boldsymbol{F}$$

The Eq. 10 represents the working force deflection equation for the element and is the base of the finite element method implemented. Knowing the expression for the element stiffness matrix $\mathbf{k}$, the nodal forces vector due to external loads $\boldsymbol{F}_E$ and the nodal forces vector due to thermal induced stress $\boldsymbol{F}_T$, the nodal displacements vector $\boldsymbol{u}_d$ is solved, upon imposing the proper constraints conditions.

The element stiffness matrix is formally given by the volume integral of Eq. 11, which is numerically approximated with a two point Gauss quadrature formula.

$$\mathbf{k} = \int_{\Delta V_0} \mathbf{B}^T \mathbf{C} \mathbf{B}\, dV \quad (11)$$

Similar considerations can be done for the nodal internal thermal loads definition, described by the following volume integral:

$$\boldsymbol{F}_T = \int_{\Delta V_0} \mathbf{B}^T \mathbf{C}\, \boldsymbol{\varepsilon}_T dV \quad (12)$$

The analysis developed till this point refers to a single element, while the solid is discretized using a large number of them. For this reason, the assembly process that constructs the master stiffness matrix $\mathbf{K}$ and master equations, related to the whole discretized solid has to be performed. This procedure is not trivial and takes advantage of the master stiffness matrix characteristics.

In particular, being **K** sparse and symmetric, the compressed column storage (CCS) technique is used. The global nodal elastic displacement vector of Eq. 5 is obtained through a conjugate gradient iterative method, after imposing the suitable essential zero constraint conditions to the system. Zero Dirichlet boundary conditions are in fact necessary to obtain a unique solution for the system of equations and to avoid rigid body motion. The rows and columns corresponding to the constrained nodes are removed from the master stiffness matrix **K**, allowing determining a static elastic deformation.

4.2 Inertia Relief

The mechanical bodies composing the rotating kit of an axial piston machine are designed to allow for relative motion. Furthermore, a micro-motion relative to the fluid film interfaces separating the mechanical bodies takes place. This micro-motion improves the load carrying capability of the fluid film, through the squeeze film effect.

Applying an arbitrary constraint to a finite element model of the moving parts could lead to a wrong answer in the determination of the elastic deformation. In fact, a reaction force would arise at the constraint which does not exist in the real situation. This force would cause unrealistic nodal elastic deflection, ultimately predicting false thermo-elastohydrodynamic fluid film geometry.

When performing the finite element analysis of a free structure, an advanced method that reduces the impact of the constraint conditions on the final solution is known as inertia relief. In this method, the applied loads are assumed not be in equilibrium and the solution to the problem is obtained introducing an accelerating coordinate system, attached to the center of mass (CG) of the structure. The applied loads are balanced by a set of translational and rotational accelerations generated by the applied loads. These accelerations provide body forces, distributed over the structure in such a way that the total sum of the applied forces on the structure is zero. This provides the steady-state stress and deformed shape in the structure as if it were freely accelerating due to the applied loads.

Essential boundary conditions for the solution of the FEM linear system are applied only to restrain rigid body motion. In particular, since the inertial accelerations are found with respect to the body CG and *d'Alembert* inertia forces are then distributed over the structure, it can be assumed that the CG is fixed to earth. Because the external loads are balanced by the inertial accelerations, the reaction forces corresponding to these boundary conditions at the CG are zero.

Considering a discretized structure with N elements, in the implementation of the inertia relief method the coordinates of the CG respect to the origin (o) are found, as shown by Eq. 13.

$$\boldsymbol{r}_{\mathrm{CG}} = \frac{1}{M} \sum_{i=0}^{N} \left(\rho_i \Delta V_i \right) \cdot \boldsymbol{r}_{io} \tag{13}$$

Where, M is the total mass of the structure, ρ_i is the density of the ith element and ΔV_i is the volume of the

i^{th} element. Knowing the coordinates of the CG, the moment of inertia tensor, **I**, of the entire structure can be determined.

$$\mathbf{I} = \sum_{i=1}^{N} \left(\rho_i \Delta V_i \right) \left(\| r_i \|^2 \mathbf{E}_3 - \begin{bmatrix} x_i^2 & x_i y_i & x_i z_i \\ y_i x_i & y_i^2 & y_i z_i \\ z_i x_i & z_i y_i & z_i^2 \end{bmatrix} \right) \tag{14}$$

Where, $\boldsymbol{r}_i = \{x_i, y_i, z_i\}$ represent the distance of the center of each element from the CG and $\mathbf{E}_3$ is the (3x3) identity matrix.

Since, it is assumed that all the applied forces and torques to the structure are balanced about the CG of the structure, solving the following equations allows determining the entire solid body inertial linear, $\boldsymbol{a}_{\mathrm{CG}}$, and rotational, $\boldsymbol{\alpha}_{\mathrm{CG}}$, accelerations at the CG.

$$\boldsymbol{a}_{\mathrm{CG}} = -\frac{1}{M} \sum_{i=1}^{N} \boldsymbol{F}_i \tag{15}$$

$$\boldsymbol{\alpha}_{\mathrm{CG}} = -\mathbf{I}^{-1} \sum_{i=1}^{N} \left(\boldsymbol{r}_i \times \boldsymbol{F}_i \right) \tag{16}$$

Where, $\boldsymbol{F}_i$ is the element applied load vector, induced by external and internal nodal forces. The resultant inertial loads deriving from these accelerations are distributed back to the structure elements, according to their specific mass and moment of inertia tensor. The fictitious inertia forces for each element, resulting from this distribution process, are assumed to be applied in the element center and uniformly applied to its nodes. In particular, each element experiences a total inertial force, which presents a linear, $\boldsymbol{F}_{ai}$, and a rotational, $\boldsymbol{F}_{ai}$, component. The linear force is shown in the following equation.

$$\boldsymbol{F}_{ai} = \left(\rho_i \Delta V_i \right) \boldsymbol{a}_{\mathrm{CG}} \tag{17}$$

The rotational force is function of the inertial angular torque, $\boldsymbol{\tau}_{\alpha i}$, which can be expressed as follows:

$$\boldsymbol{\tau}_{\alpha i} = \mathbf{I}_i \boldsymbol{\alpha}_{\mathrm{CG}} \tag{18}$$

Where, $\mathbf{I}_i$ is the moment of inertia tensor for the ith element. Taking advantage of the properties of the vector triple cross product, an expression for the rotational force can be obtained:

$$\boldsymbol{\tau}_{\alpha i} \times \boldsymbol{r}_i = \left(\boldsymbol{r}_i \times \boldsymbol{F}_{\alpha i} \right) \times \boldsymbol{r}_i = -\left(\boldsymbol{r}_i \cdot \boldsymbol{F}_{\alpha i} \right) \boldsymbol{r}_i + \left(\boldsymbol{r}_i \cdot \boldsymbol{r}_i \right) \boldsymbol{F}_{\alpha i} \tag{19}$$

Being the force $\boldsymbol{F}_{\alpha i}$ associated to a rotation, it is assumed to be orthogonal to the element center position vector, $\boldsymbol{r}_i$. This assumption causes the dot product $\boldsymbol{r}_i \cdot \boldsymbol{F}_{\alpha i}$ to be zero and the rotational force can be derived from Eq. 19 as:

$$\boldsymbol{F}_{\alpha i} = \frac{\boldsymbol{\tau}_{\alpha i} \times \boldsymbol{r}_i}{\| \boldsymbol{r}_i \|^2} \tag{20}$$

Therefore, considering also the inertial loads acting on the entire structure in the master linear system of equations, it is possible to write:

$$\mathbf{K} \cdot \boldsymbol{u}_{\mathrm{d}} = \boldsymbol{F}_{\mathrm{E}} + \boldsymbol{F}_{\mathrm{T}} + \boldsymbol{F}_{\mathrm{IR}} \tag{21}$$

Where, $\boldsymbol{F}_{\mathrm{IR}}$ represents the nodal load vector containing the inertial linear and rotational contribution of each

element to balance the applied loads. The solution of the system is obtained after the imposition of zero displacement constraint conditions on the nodes closer to the CG of the structure only to avoid rigid body motion.

5 Numerical Results

In this section, the impact of the inertia relief method over the standard zero displacement constraint method is discussed through the finite element analysis on the main bodies of an axial piston machine. In addition, a fully-coupled simulation using inertia relief to predict elastic deformations of the solid bodies is shown for the piston/cylinder interface.

5.1 Axial Piston Machine Mechanical Bodies

Finite element analysis on the three main moving bodies of an axial piston machine are discussed, considering the typical pressure loading conditions used in the fully-coupled modeling. The elastic deformation from a suitable zero displacement constraint condition and from the inertia relief technique is compared for each of the discretized solid bodies. A special focus is given to the surface elastic deformations corresponding to the sealing surfaces of the bodies, since they directly affect the fluid film geometry. For simplicity, all the parts are considered made of standard steel presenting a Young modulus, E, of 210 GPa and a Poisson ratio, v, of 0.27.

5.1.1 Piston

Two different types of loading conditions on the piston body have been considered and are depicted in Fig. 7. On the left, the loading condition corresponding to a face on the piston sealing surface, highlighted in red, is shown. The face is loaded with a reference pressure of 100 bar. The result of this analysis is important because, as explained in the previous sections (Eq. 6), the influence matrices generation is based on combining elastic deformations obtained from this loading principle. Without inertia relief, the nodes constrained with a zero displacement are the ones on the surface closer to the piston axis, highlighted in blue.
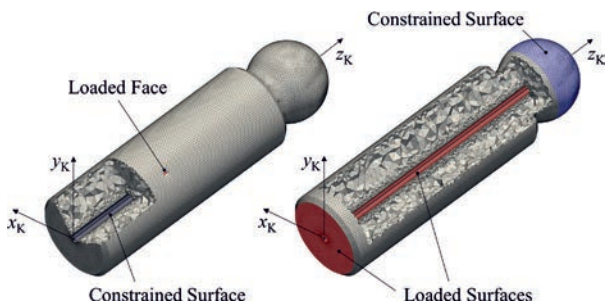
Fig. 7: *Piston loading and constraint conditions for one face on piston sealing surface (left) and for surfaces exposed to displacement chamber pressure (right)*

On the right of Fig. 7, the loading and constraint conditions corresponding to a pressure load of 100 bar on the surfaces typically exposed to displacement chamber pressure are presented.
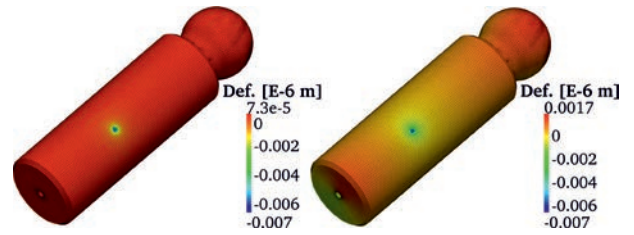
Fig. 8: *Piston exaggerated radial elastic deformation for zero displacement constraint (left) and inertia relief (right) due to 100 bar radial face load*

The loaded surfaces are highlighted in red, while the color blue is used to define the constrained nodes. For this loading condition, the nodes on the outer surface in contact with the slipper socket are fully constrained when not considering the inertia relief.

Referring to Fig. 8, the radial elastic deformations resulting from the application of a local load on one face of the piston surface (i.e. one influence matrix) are shown. The piston view is exaggerated to emphasize the localized piston elastic deflections. It can be noticed how, the piston on the left of Fig. 8, constrained with a zero displacement boundary condition on the nodes closer to the piston axis, presents a very localized surface elastic deformation. The highest elastic deformation corresponds to the point of application of the compressing pressure force. Differently, the piston on the right of Fig. 8 is studied applying the inertia relief method, therefore the external localized pressure load on the same face is balanced by the induced inertial acceleration field. It can be noticed how, for a similar local deformation the piston tends to bend in a direction opposite to the compressive pressure load. This is a result of the inertial forces distributed on the solid structure which are generated to balance the external applied load. This inertial forces cause a non-negligible elastic surface deformation of the regions distant from the loaded face, which will affect the fluid film overall geometry.

Similar different results can be found if referring to Fig. 9, where the finite element analysis have been performed on the piston body loaded with 100 bar displacement chamber pressure.
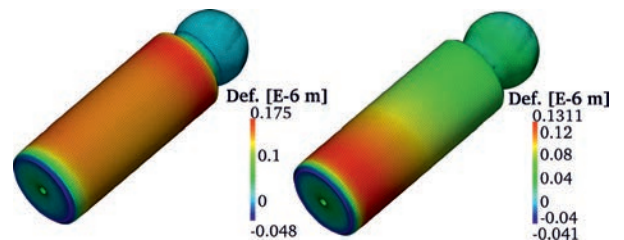
Fig. 9: *Piston exaggerated radial elastic deformation for zero displacement constraint (left) and inertia relief (right) due to 100 bar DC surfaces load*

On the left of Fig. 9, the piston presenting a zero displacement constraint on the piston head surface nodes is shown. It can be noticed, from the exaggerated view, how the piston tends to significantly compress axially towards the constrained head. The result of this compression is a radial surface elastic deformation presenting a peak of 0.175 μm closer to the constrained head. On the right of Fig. 9, the piston subjected to the

same type of load but analyzed using inertia relief is shown. It can be noticed how, being the reaction at the constraint disappeared; the overall axial compression is significantly less. In addition, the radial surface elastic deformations, ultimately affecting fluid film thickness, are lower and present a different distribution.

5.1.2 Slipper

Similar finite element analysis has been performed on the slipper body, considering two different types of loading conditions. In one case, one face of the slipper sealing surface is loaded with 100 bar pressure. On the other case, the slipper surfaces normally exposed to displacement chamber pressure (pocket) are loaded with 100 bar. In both conditions, the slipper socket surface is fully constrained and compared with analysis executed using the implemented inertia relief method.

The loading and zero displacement constraint conditions for the slipper finite element analysis are shown in Fig. 10.
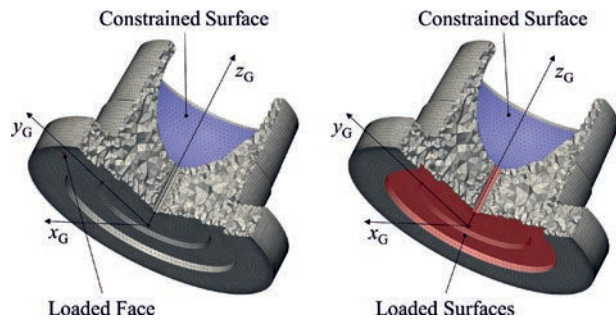
Fig. 10: *Slipper loading and constraint conditions for one face on slipper sealing surface (left) and for surfaces exposed to displacement chamber pressure (right)*

The results from face loading for the standard socket surface constraint and the inertia relief method are shown in Fig. 11, where exaggerated slipper views are overlaid to a non-deformed transparent slipper. The elastic deformation of the sealing surface in *z*-direction, corresponding to the fluid film thickness direction, is higher when the socket is strictly constrained (left). The inertia relief influence on the surface elastic deflection of the slipper sealing area is clearly visible on the right of Fig. 11.
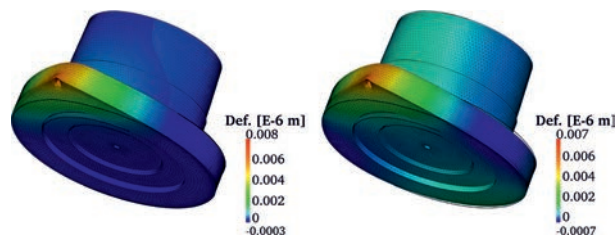
Fig. 11: *Slipper exaggerated z-axis elastic deformation for zero displacement constraint (left) and inertia relief (right) due to 100 bar face load on sealing surface*

The inertial accelerations reduce the local deformation and cause part of the remaining slipper surface area to deflect in the opposite direction of the pressure force. This effect has a potential strong influence on the slipper fluid film geometry.
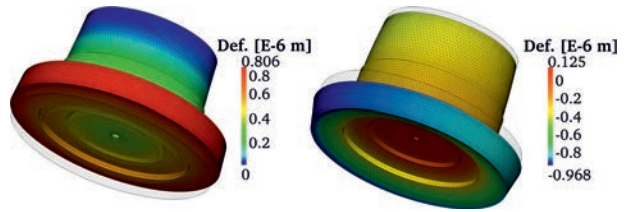
Fig. 12: *Slipper exaggerated z-axis elastic deformation for zero displacement constraint (left) and inertia relief (right) due to 100bar pocket surfaces load*

Inertia relief method has a major impact on slipper sealing land surface deformation when considering the pressure loads acting on the slipper pocket surfaces.

Referring to Fig. 12, on the left the elastic deformation of the slipper structure when the socket is fully constrained is depicted. The body compresses under the pressure force acting normally to the pocket surface if compared to the transparent non-deformed configuration. This effect theoretically increases the clearance between slipper and swash plate. The inertia relief effect (right) shows how the inertial forces, necessary to balance the pressure loads, strongly reduce the solid body compression. An elastic deflection of the sealing surface in the opposite direction induces a theoretical reduction of the slipper/swash plate fluid film thickness, which would contribute to an increment of the hydrodynamic pressure build up below the sealing surface, directly affecting the slipper dynamics. It should be noticed that the displacement pressure load transferred from the piston is an additional load component acting on the slipper body, which is not presented in this paragraph.

5.1.3 Cylinder Block

Due to its mass and to the major pressure loads acting on it from the displacement chambers, the inertia relief method presents a strong influence on the cylinder block finite element analysis. One displacement chamber is loaded in this study with 100 bar reference pressure. As shown in Fig. 13, the cylinder bock loaded surfaces are highlighted in red. Zero displacement constraints are assigned, when not using inertia relief, to the typically splined surface (blue).
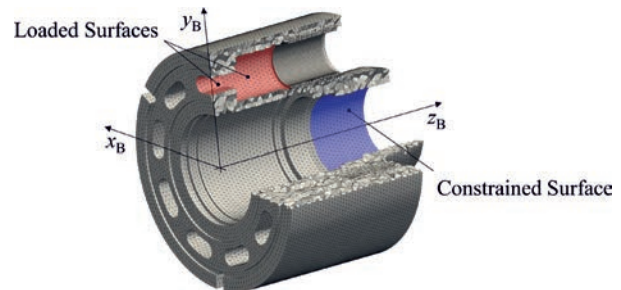
Fig. 13: *Cylinder block loading and constraint conditions for one displacement chamber*

The external pressure force acting in the displacement chamber causes the entire block to bend around the constrained splined surface, as shown by the left of Fig. 14.
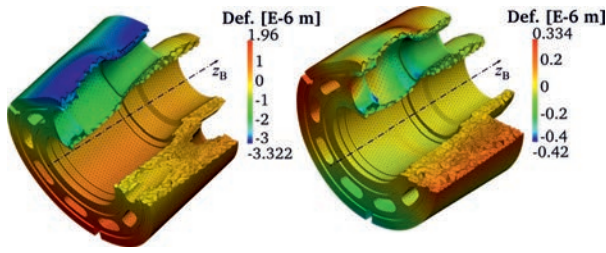
Fig. 14: *Cylinder block exaggerated z-axis elastic defor-mation for zero displacement constraint (left) and inertia relief (right) due to 100bar load*

This bending generates an elastic deformation of the cylinder block sealing land in *z*-direction directly affecting the fluid film thickness of this interface. The same elastic deformation is not visible when performing the analysis with inertia relief. The cylinder block does not bend thanks to the balancing action of the inertial loads and a different sealing land elastic deformation distribution is obtained. The influence of the constraint conditions on the static analysis is removed.

6 Piston/Cylinder Interface Fully-Coupled Simulation and Measurement Comparisons

To assess the validity of the inertia relief method and to understand its impact on the fluid film performance, in this section the fully-coupled model is used to simulate the non-isothermal fluid film flow conditions between piston and cylinder of an axial piston pump designed to allow cylinder friction force measurements on one of the pistons of the rotating block. This test pump, referred as *Tribo Pump*, exactly replicates the behavior of a nine piston axial piston pump, but has been designed to measure the friction forces in axial and tangential direction between the piston/cylinder (Ivantysynova and Lasaar, 2004). In particular, the measured friction force is the one acting on the cylinder surface. The instantaneous displacement chamber pressure is also measured. A telemetry system allows transferring the sensors signals from the rotating group to the data acquisition system.
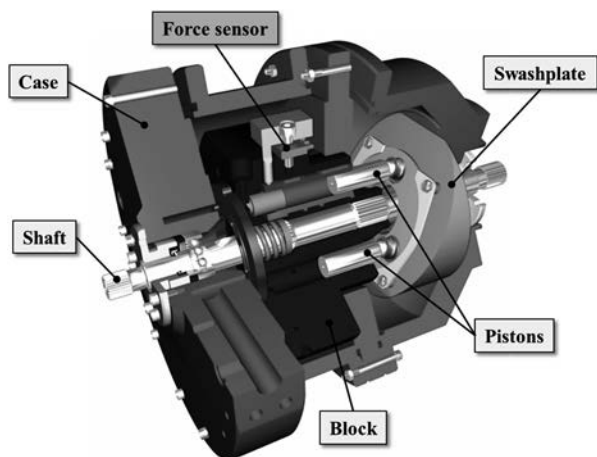
Fig. 15: *Tribo test rig pump assembly*

Fig. 15 shows the design of this special pump, which has a fixed swash plate angle of 17°. The cylinder block is oversized compared to a standard one to accommodate the force measurement system.

Only three main pistons are reciprocating in the block, while other five balancing pistons are located on the block outer circumference to compensate the external forces unbalance. One of the three main moves in a hydrostatically balanced brass bushing, decoupled from the steel cylinder block.

The brass bushing transfers the axial and circumferential viscous friction forces exerted on the bushing through a lever to the piezoelectric force sensor.
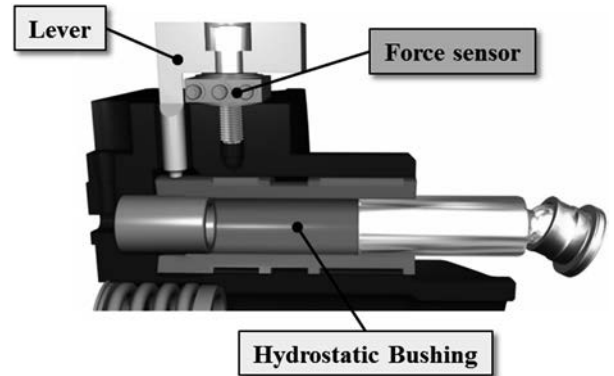
Fig. 16: *Hydrostatic cylinder and sensor*

A closer representation of the brass bushing design is shown in Fig. 16. The pockets on the outer circumference of the brass bushing are pressurized with displacement chamber pressure, which guarantees the hydrostatic bearing function.

Table lists the material properties for the test rig steel piston and brass cylinder mechanical parts, which are used as input to the fully-coupled fluid structure model.

Table 1: Tribo pump material properties

Material property	Piston	Bushing
ρ [kg/m³]	7800	8600
E [GPa]	210	130
ν [-]	0.27	0.32
α_T [E-6/°C]	12	21
λ [W/m°C]	54	105

These parameters are critical because they directly affect the thermal behavior and fluid-structure interaction of the piston/cylinder interface. The piston/cylinder assembly numerical environment, with the discretized solids for this simulation study, is depicted in Fig. 17. The geometry of the actual piston and bushing are precisely replicated from CAD solid models and meshed.

The measured oscillating displacement chamber pressure is used as boundary for non-isothermal fluid film flow, piston force balance and surface elastic deformation calculations. It represents one of the key boundaries for the simulation, being the most significant oscillating force influencing the piston micro-

motion. Different heat transfer boundaries are implemented for the piston/cylinder assembly. In particular, the fluid film surfaces are assigned a *Neumann* boundary, being the heat flux from the fluid film determined by the non-isothermal fluid film model.
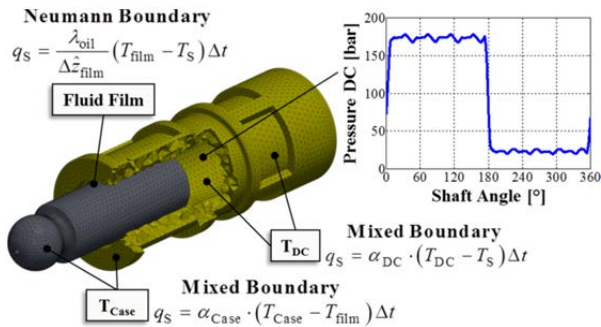
Fig. 17: *Tribo test rig piston/cylinder discretization and boundaries*

Table 2: Mixed boundaries convection coefficients

Displacement chamber α_{DC} [W/m^2°C]	3000
Rotating kit case α_{Case} [W/m^2°C]	2000
Block/valve plate fluid film α_{CB} [W/m^2°C]	1000

All the other surfaces of the piston and of the bushing are considered to be a *Mixed* boundary, assuming forced convection to better describe the heat transfer in those regions. Convection coefficients for the different boundary surfaces are shown in Table.

The numerical analysis has been performed considering two operating conditions corresponding to measured cases. The main parameters from the simulations are reported in Table. The purpose of the numerical analysis is to demonstrate the capability of the fully-coupled model to capture the viscous friction force behavior over one shaft revolution, evaluating the influence of the different constraint conditions.

Table 3: Tribo pump measured and simulated operating conditions

Operating Conditions	**1**	**2**
Differential pressure Δp [bar]	101.7	130.0
Low pressure p_{LP} [bar]	19.3	21.0
Shaft angular speed ω [rpm]	1000	1000
Case temperature T_{Case} [°C]	49.3	50.6
High pressure temp. T_{HP} [°C]	45.4	44.1
Low pressure temp. T_{LP} [°C]	43.5	41.9

The solid parts constraint conditions play a very important role in the determination of the pressure and thermal elastic deformations. For these reasons, the fully/coupled simulations have been run considering both zero displacement constraint conditions and inertia relief (*IR*).
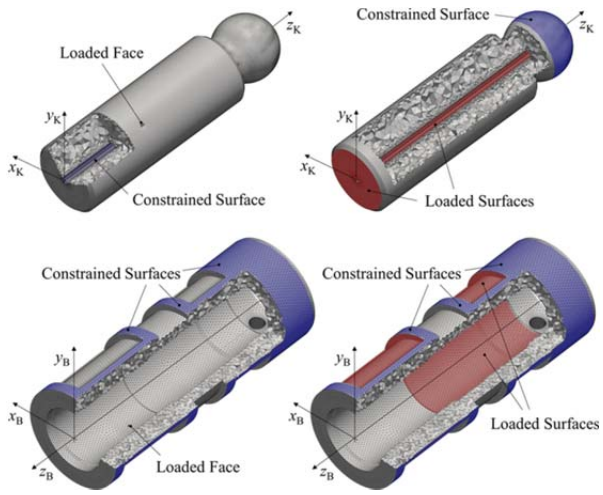
Fig. 18: *Piston (top) and brass bushing (bottom) loading and constraint conditions for one face on sealing surface (left) and for surfaces exposed to DC pressure (right)*

In case of zero displacement constraint conditions, mesh nodes must be constrained to avoid rigid body motion. Fig. 18 shows the loaded and constrained surfaces for the piston and brass bushing solid bodies when calculating pressure induced elastic deformations. Proper degrees of freedom are removed to obtain constrain conditions representing reality as close as possible. The piston is in fact unconstrained during normal operation of an axial piston pump and in case of full film lubrication is sustained and consequently loaded only by fluid film pressure. The brass bushing is theoretically completely free to move thanks to the hydrostatic bearing.

The comparison of the fully-coupled simulations with the measured axial friction forces allows determining the impact of this advanced constraint method on the numerical results. The behavior of the fluid film is also analyzed considering the main physical variables affecting its performance over one shaft revolution.

6.1 Operating Condition 1

This operating condition, which is characterized by a high pressure of 120 bar, represents a moderate load for the test pump. The axial viscous friction force acting on the hydrostatic bushing is a result of the combined contributions from the pressure differential across the piston (Poiseuille component) and from the piston relative motion (Couette component). Additionally, the complex oscillating shape assumed by the piston/cylinder fluid film thickness directly affects the generated axial viscous friction force. During the first 180° of shaft angle the piston is pumping fluid, hence it is subjected to high displacement chamber pressure, while the suction phase at low pressure takes place during the next 180°.
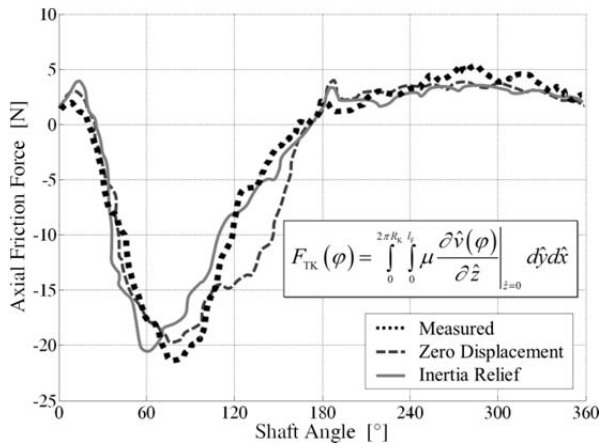
Fig. 19: *Axial viscous friction force comparison for operating condition 1*

The axial viscous friction force prediction for this operating condition obtained by the two model combinations is shown in Fig. 19. Both the constraint conditions allow capturing the friction force behavior during the critical delivery stroke.

However, at this moderate load conditions, the combination of the inertia relief constraint method coupled with pressure induced deformations and thermal effects does not play a significant role in generating more precise numerical results if compared to a zero displacement constraint method. In particular, the magnitude of the axial friction force is well predicted by both models.

6.2 Operating Condition 2

This operating condition represents the highest considered load, with a high pressure of 151 bar. The impact of fluid-structure interaction and thermal effects is more significant at this point; due to the fluid film more critical conditions to bear the external oscillating loads acting on the piston.
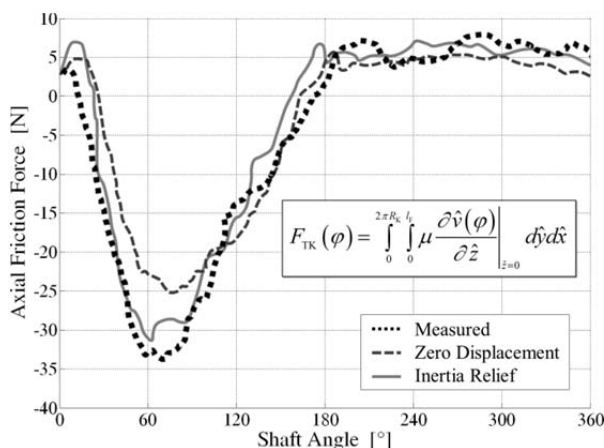
Fig. 20: *Axial viscous friction force comparison for operating condition 2*

Referring to Fig. 20, the simulated axial viscous friction forces are compared with the measured curve. It can be noticed how the solid model based on zero displacement constraint boundaries diverges from the real parts conditions as the external load increases, underpredicting the axial friction forces during the

pumping stroke. For this operating condition, the superior accuracy provided by the combination of the advanced inertia relief constraint method coupled with pressure induced deformations and thermal effects plays a key role in generating more precise numerical results.
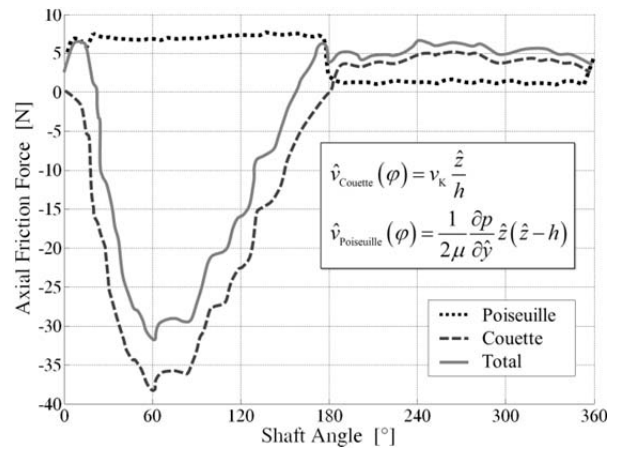
Fig. 21: *Simulated axial friction force components for operating condition 2*

Hence, inertia relief method becomes more important at high loads, to accurately replicate the solid bodies unconstrained characteristics. In addition, Fig. 21 shows the components of the axial viscous friction force for the most accurate model together with the resulting total friction force. This analysis allows decoupling the impact of the two main physical phenomena generating viscous friction in the interface, i.e. Couette and Poiseuille contributions.
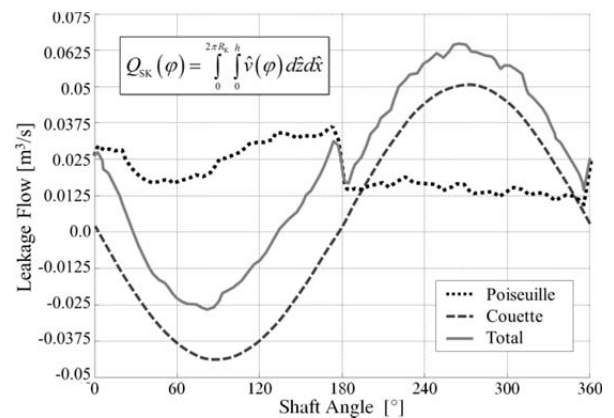
Fig. 22: *Simulated leakage across the piston/cylinder interface for operating condition 2 (negative leakage towards the displacement chamber in $-z_K$ direction)*

The leakage flow across the piston/cylinder interface represents another critical variable defining the fluid film performance over one shaft revolution. The fully-coupled model allows evaluating the fluid film flow as well considering the impact of the thermo-elastohydrodynamic phenomena described so far. In particular, Fig. 22 shows the piton/cylinder interface leakage flow and its two components over one shaft revolution for this operating point.

Friction forces and leakages represent the two main sources of energy dissipation for the fluid film interface. Their development over one shaft revolution of

the machine is strictly related to the interface performance and to the dynamic behavior of the fluid film interacting with the boundary structures. Therefore, for this operating condition, thanks to the fully-coupled model, the piston/cylinder fluid film thermo-elastohydrodynamic behavior is studied. Considering the numerical results obtained with inertia relief, the most significant physical fields defining the interface performance over one shaft revolution are analyzed using an unwrapped Cartesian coordinate system, as shown by Fig. 23.

$$\hat{x} = \phi_K R_Z \qquad \hat{y} = l_F \qquad \hat{z} = h(\varphi, t)$$
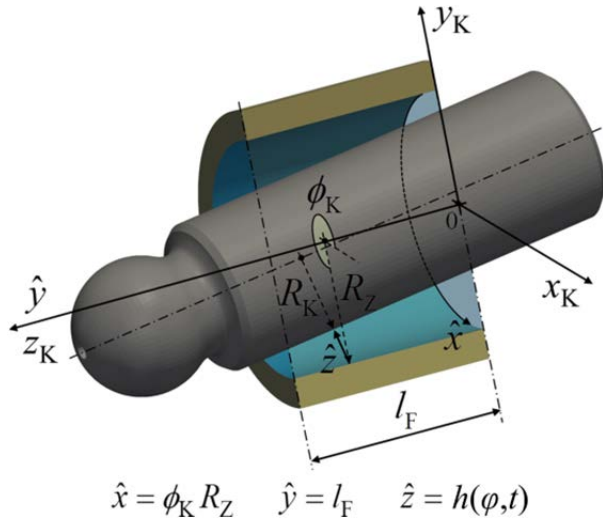
Fig. 23: *Piston/cylinder interface unwrapped Cartesian coordinate system definition*

Referring to Fig. 24, the oscillating thermo-elastohydrodynamic fluid film geometry at discrete shaft angles is depicted.
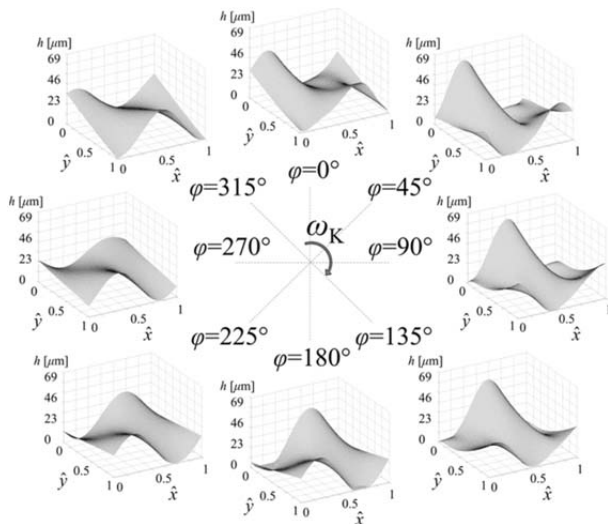
Fig. 24: *Piston/cylinder interface unwrapped thermo-elastohydrodynamic fluid film thickness over one shaft revolution using inertia relief*

Regions of low film thickness are present during the high pressure stroke, where the piston inclines the most due to the high external loads. During the suction stroke, the load on the piston decreases and the sliding motion takes place almost coaxially with the cylinder bore. The regions of lower fluid film thickness are characterized by high pressure peaks and are responsi-

ble for the strong fluid-structure interaction, as shown by Fig. 28. A correspondence between piston micro-motion and fluid film pressure field dynamics is clearly visible.
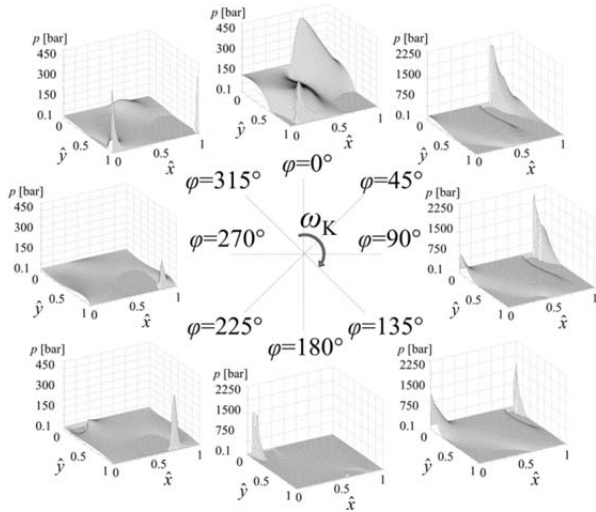
Fig. 25: *Piston/cylinder interface unwrapped thermo-elastohydrodynamic pressure field over one shaft revolution using inertia relief*

Furthermore, the fluid film behavior is affected by the pressure and thermal elastic deformations, which change continuously over one shaft revolution. The dynamic behavior of the surface elastic deformations is influenced by piston micro and macro motions.
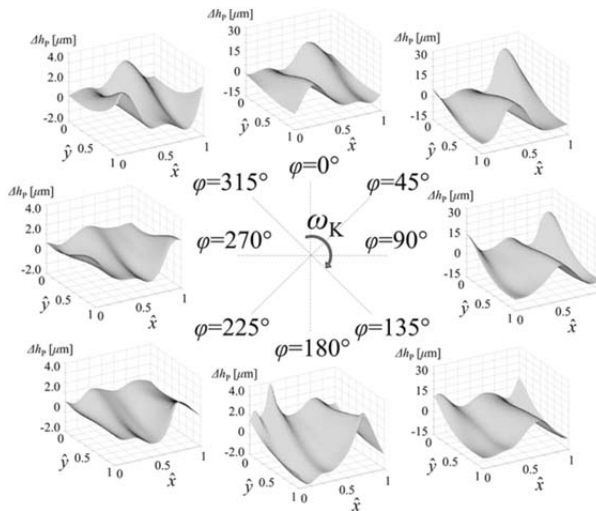
Fig. 26: *Piston/cylinder interface unwrapped pressure induced elastic deformations over one shaft revolution using inertia relief*

Referring to Fig. 28, the total pressure elastic deformation directly modifying the fluid film geometry is presented. The elastic deformation fields combine the contribution of piston and cylinder surface to the fluid film geometry alteration. The inertial forces balancing the external loads contribute as well to the surface elastic deformation. The fluid film geometry is modified also by the surface elastic deformations due to the thermal expansion of the piston and the cylinder. The steady state thermal surface elastic deformations are superimposed to the dynamic pressure elastic defor-

mations. The relative motion of the piston causes the piston sealing surface to slide relative to the fluid film, periodically modifying the thermal deformation field seen by the fluid film.
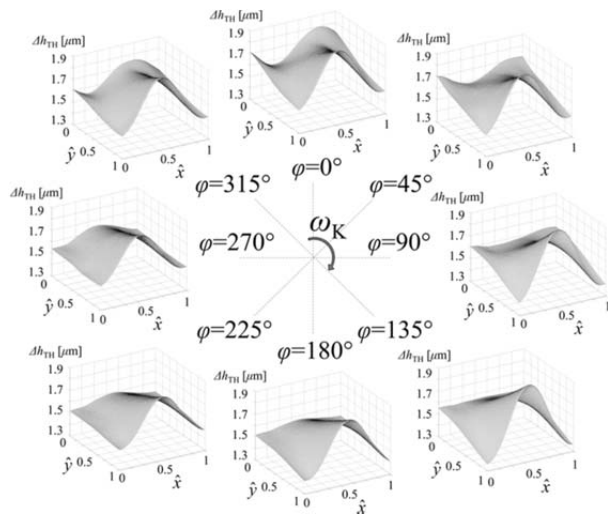
Fig. 27: *Piston/cylinder interface unwrapped thermal elastic deformations over one shaft revolution*

The total thermal elastic deformation altering the fluid film geometry over one shaft revolution is shown by Fig. 27. The thermal deformation fields couple the contribution of piston and cylinder expansions due to the uneven solids temperature gradients.

The fluid film flow solution is obtained considering non-isothermal conditions, where the influence of the solids boundary temperature is very important for an accurate result. In fact, the fluid film is bounded by the piston and cylinder sealing surfaces. The heat transfer calculations allow predicting the solid bodies temperature distributions, hence the fluid film boundary temperatures. Referring to Fig. 28, the predicted temperature distributions of the piston and the bushing for this operating condition are shown.
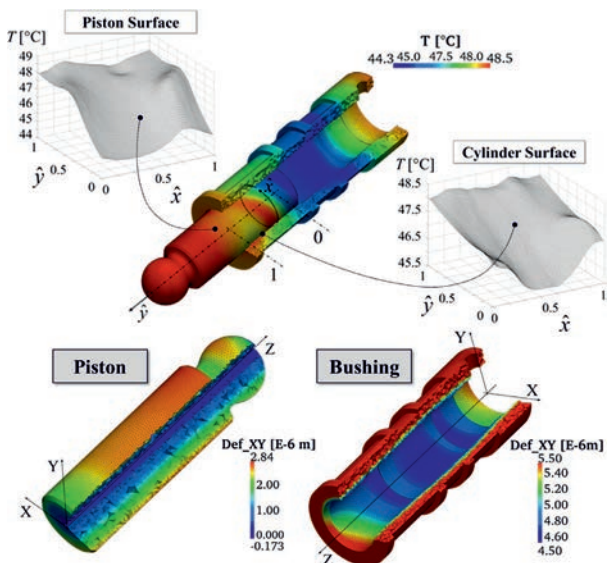
Fig. 28: *Piston/cylinder assembly temperature distribution (top) and fluid film boundary surfaces radial thermal elastic deformation (bottom) for operating condition 2*

The unwrapped fluid film surface temperatures are depicted as well. Furthermore, Fig. 28 shows the temperature induced radial elastic deformations for the mechanical parts, which are combined and interpolated to the fluid film at each time step. The magnitude of these surface thermal elastic deformations is comparable with the fluid film thickness of the interface. Hence, these physical phenomena play a critical influence on the Tribo Pump piston/cylinder overall fluid film performance.

Finally, it should be noticed how the magnitude of the boundary temperatures, determined by the laboratory test conditions, is significantly lower than the typical operating temperatures of an axial piston unit. Therefore, the influence of thermo-elastohydrodynamic phenomena on the piston/cylinder fluid film performance of standard axial piston machines, characterized by more extreme and more complex boundaries in terms of displacement chamber pressure and surrounding temperatures, cannot be neglected.

7 Conclusions

An advanced method to calculate the elastic deformations affecting the main mechanical bodies of axial piston machines has been presented in this paper. The main moving parts of an axial piston machine rotating kit are in fact not firmly constrained, presenting a significant numerical issue when performing a finite element analysis. An accurate prediction of the elastic deformation of the solid bodies is crucial to determine the axial piston machines fluid film interfaces behavior. The implemented technique, known as inertia relief, expands in fact the capabilities of the fully-coupled thermo-elastohydrodynamic model for the lubricating interfaces of axial piston machines developed by the authors' research group.

The inertia relief method allows reducing the influence of zero displacement constraint conditions on the solution of a finite element linear system of elastic equations. It is assumed that the external applied loads acting on the solid structure are balanced by an inertial acceleration field induced by the applied loads. The method therefore allows simulating unconstrained structures in a static elastic analysis and is suitable to replicate the real design characteristics of axial piston machines moving mechanical parts.

Numerical results on the surface elastic deformation of typical rotating kit solid structures are shown. The impact of inertia relief for the same type of applied external pressure load is shown to be significant compared to a zero displacement constraint condition, especially for the cylinder block and the slipper bodies. Furthermore, fully-coupled simulations on the piston/cylinder interface of a special design test pump, capable of measuring the piston/cylinder friction forces, are presented. The comparison of the numerical results with piston/cylinder interface friction force measurements shows the improvement in model accuracy obtained considering inertia relief method when solving for the mechanical parts pressure induced elastic deformation especially at higher load conditions.

Additionally, the piston/cylinder fluid film fields dynamic behavior is shown, when considering inertia relief, by presenting the dynamic performance of the most critical fields over one shaft revolution. The magnitude of surface elastic deformations related to thermo-elastohydrodynamic phenomena cannot be neglected and directly affects the piston/cylinder interface dynamics.

Nomenclature

a_{CG}	Linear acceleration vector	[m/s^2]
B	Strain-displacement matrix	[-]
c_p	Fluid heat capacity	[J/kgK]
C	Constitutive matrix	[-]
CB	Cylinder block/valve plate film	[-]
dV	Differential volume	[m]^3
DC	Displacement chamber	[-]
E	Elastic modulus	[GPa]
F_{TK}	Axial viscous friction force	[N]
F_i	Total element force vector	[N]
F_{ai}	Linear inertial force	[N]
$F_{\alpha i}$	Rotational inertial force	[N]
F_{IR}	Inertial load vector	[N]
F_E	External load vector	[N]
F_T	Thermal load vector	[N]
HP	High pressure	[-]
h	Film thickness	[m]
IM_i	Influence matrix surface face	[m]
IM_{DC}	Influence matrix DC surfaces	[m]
I	Solid moment of inertia tensor	[kgm^2]
I_i	Element moment of inertia tensor	[kgm^2]
k	Element stiffness matrix	[N/m]
K	Body master stiffness matrix	[N/m]
N	Total number of finite elements	[-]
n	Element node number	[-]
p	Fluid pressure	[Pa]
p_{ref}	Fluid reference pressure	[Pa]
p_{DC}	Displacement chamber pressure	[Pa]
p_{HP}	Delivery port pressure	[Pa]
p_{LP}	Suction port pressure	[Pa]
Q_S	Solid body heat flux	[W/m^2]
Q_{TK}	Piston/cylinder leakage flow	[m^3/s]
r	Position vector	[m]
T	Fluid temperature	[°C]
T_B	Solid body temperature	[°C]
T_{Case}	Case fluid temperature	[°C]
T_{HP}	High pressure fluid temperature	[°C]
T_{LP}	Low pressure fluid temperature	[°C]
u_d	Displacement vector	[m]
V	Fluid velocity vector	[m/s]
$\hat{x}, \hat{y}, \hat{z}$	Piston unwrapped coordinates	[m]
α_{CG}	Rotational acceleration vector	[rad/s^2]
α_T	Thermal expansion coefficient	[E-6/°C]
α_{DC}	DC convection coefficient	[W/m^2°C]
α_{Case}	Case convection coefficient	[W/m^2°C]
α_{CB}	CB convection coefficient	[W/m^2°C]
ε	Total elastic strain	[-]
ε_F	Elastic strain vector	[-]
ε_T	Thermal strain vector	[-]
μ	Fluid dynamic viscosity	[Pa·s]
ρ	Fluid density	[kg/m^3]
ρ_i	Solid finite element density	[kg/m^3]
λ	Solid thermal conductivity	[W/m°C]
ω	Shaft speed	[rad/s]
ν	Poisson ratio	[-]
Φ_D	Mechanical dissipation	[W/m^3]
$\tau_{\alpha i}$	Inertial angular torque	[Nm]
Δh	Deformation vector	[m]
ΔV_i	Solid finite element volume	[m^3]
$\nabla \cdot$	Divergence	[-]
∇	Gradient	[-]

References

Hintz, R. 1975. Analytical Methods in Component Modal Synthesis. *AIAA Journal,* Vol. 13, No. 8, pp. 1007 - 1016.

Fatemi, A., **Wohlers, A.** and **Murrenhoff, H.** 2008. Simulation of Elastohydrodynamic Contact between Piston and Cylinder in Axial Piston Pumps. *Proc. of the 6th International Fluid Power Conference*, Dresden, pp. 539 - 552.

Felippa C. and **Clough R.** 1969. *The Finite Element Method in Solid Mechanics*. SIAM-AMS Proceedings II, American Mathematical Society, Providence, pp. 210 - 252

Hartley G. 1986. *Fundamentals of the Finite Element Method.* Macmillan Publishing Company. New York.

Huang C. and **Ivantysynova M.** 2006. An advanced gap flow model considering piston micro motion and elastohydrodynamic effect. *Proc. of the 4th FPNI Phd Symposium*, Sarasota, Florida.

Ivantysynova, M. 1985. Temperaturfeld im Schmierspalt zwischen Kolben und Zylinder einer Axialkolbenmaschine. *Maschinenbautechnik* 34, pp. 532 - 535.

Ivantysynova, M. and **Huang, Ch.** 2002. Investigation of the gap flow in displacement machines considering the elastohydrodynamic effect. *5th JFPS International Symposium on Fluid Power*. Nara, Japan. pp. 219 - 229.

Ivantysynova, M., **Huang, C.** and **Behr, R.** 2005. Measurements of elastohydrodynamic pressure field in the gap between piston and cylinder. *Bath Workshop on Power Transmission and Motion Control PTMC 2005*, Bath, UK, pp. 451 - 465.

Ivantysynova, M., **Huang, C.** and **Japing, A.** 2006. Determination of gap surface temperature distribution in axial piston machines. *Proc. of the 2006 ASME International Mechanical Engineering Congress*, IMECE2006-15249.

Ivantysyn J. and **Ivantysynova M.** 2001. *Hydrostatic Pumps and Motor, Principles, Designs, Performance, Modeling, Analysis, Control and Testing.* New Delhi. Academic Books International.

Kim, K. and **Sadeghi, F.** 1992. Three-dimensional temperature distribution in EHD lubrication: Part I - circular contact. *ASME Journal of Tribology*, 114, pp. 32 - 41.

Kim, K. and **Sadeghi, F.** 1993. Three-dimensional temperature distribution in EHD lubrication: Part II - point contact and numerical formulation. *ASME Journal of Tribology*, 115, pp. 36 - 45.

Kleist, A. 1996. Auslegung von hydrostatischen Dicht-stellen in hydraulischen *Maschinen mit Hilfe eines Simulationswerkzeuges*. 12. AFK, Aachen.

Kleist, A. 1997. Design of Hydrostatic Static Bearing and Sealing Gaps in Hydraulic Machines. *5ᵗʰ Scandinavian International Conference on Fluid Power*, Lingköping.

Murthy, J. 2002. *Numerical Methods in Heat, Mass and Momentum Transfer.* School of Mechanical Engineering, Purdue University, West Lafayette, IN.

Pelosi, M. and **Ivantysynova, M.** 2009. A Novel Thermal Model for the Piston/Cylinder Interface of Piston Machines. *Bath ASME Symposium on Fluid Power and Motion Control* (FPMC2009), Hollywood, USA.

Pelosi, M. and **Ivantysynova, M.** 2010. A Simulation Study on the Impact of Material Properties on Piston/Cylinder Lubricating Gap Performance. *Proc. of the 6th FPNI PhD Symposium*, West Lafayette, IN, USA.

Pelosi, M. and **Ivantysynova, M.** 2010. A Fully Coupled Thermo-Elastic Model for the Rotating Kit of Axial Piston Machines. *Bath ASME Symposium on Fluid Power and Motion Control* (FPMC2010), Bath, UK.

Pelosi, M. and **Ivantysynova, M.** 2011. The Influence of Pressure and Thermal Deformation on the Piston/Cylinder Interface Film Thickness. *52ⁿᵈ IFPE Conference on Fluid Power*, Las Vegas, USA.

Pelosi, M. and **Ivantysynova, M.** 2011. Surface Deformations Enable High Pressure Operation of Axial Piston Pumps. *Bath ASME Symposium on Fluid Power and Motion Control* (FPMC2011), Washington, USA.

Pelosi, M. and **Ivantysynova, M.** 2011. A Geometric Multigrid Solver for the Piston/Cylinder Interface of Axial Piston Machines. *Tribology Transactions*, Vol. 55, No. 2, pp. 163 - 174.

Pelosi, M. and **Ivantysynova, M.** 2012. Heat Transfer and Thermal Elastic Deformation Analysis on the Piston/Cylinder Interface of Axial Piston Machines. *ASME Journal of Tribology*, Vol. 134, No. 4, [DOI: 10.1115/1.4006980].

Sadeghi, F. and **Dow, T. A.** 1987. Thermal Effects in Rolling/Sliding Contacts: Part 2-Analysis of Thermal Effects in Fluid Film. *ASME Journal of Tribology*, Vol. 109, pp. 512–518.

Wieczorek, U. and **Ivantysynova, M.** 2002. Computer Aided Optimization of Bearing and Sealing Gaps in Hydrostatic Machines - The Simulation Tool CASPAR. *International Journal of Fluid Power*, Vol. 3, No. 1, pp. 7 - 20.

Ivantysynova, M. and **Lasaar, R.** 2004. An investigation into micro- and macro-geometric design of piston/cylinder assembly of swash plate machines. *International Journal of Fluid Power*, Vol. 5, No. 1, pp. 23 - 36.

Lasaar, R. and **Ivantysynova, M.** 2002. Advanced gap design - basis for innovative displacement machines. *Proc. of 3ʳᵈ IFK Internationales Fluidtechnisches Kolloquium*, pp. 215 - 230, Aachen, Germany.

Matteo Pelosi
Born on December 29th 1982 in Parma (Italy). He received his B.Sc. and M.Sc. in Mechanical Engineering from University of Parma (Italy) in 2005 and 2007 respectively. In February 2012 he obtained his Ph.D. degree in Fluid Power from Purdue University (USA). The design and modelling of hydraulic systems has been his main research area, both at a system and a component level. His Ph.D. research focused on discovering the physical behavior of hydrostatic piston machines fluid film interfaces, through the generation of advanced fluid-structure interaction and thermal numerical models. Starting from March 2012, he joined Öhlins Racing AB (Sweden).

Monika Ivantysynova
Born on December 11th 1955 in Polenz (Germany). She received her MSc. Degree in Mechanical Engineering and her PhD. Degree in Fluid Power from the Slovak Technical University of Bratislava, Czechoslovakia. After 7 years in fluid power industry she returned to university. In April 1996 she received a Professorship in fluid power & control at the University of Duisburg (Germany). From 1999 until August 2004 she was Professor of Mechatronic Systems at the Technical University of Hamburg-Harburg. Since August 2004 she is Professor at Purdue University, USA. Her main research areas are energy saving actuator technology and model based optimization of displacement machines as well as modeling, simulation and testing of fluid power systems. Besides the book "Hydrostatic Pumps and Motors" published in German and English, she has published more than 80 papers in technical journals and at international conferences.